Flow Structures Around a Flapping-Wing Micro Air Vehicle Performing a Clap-and-Peel Motion

Perçin, Mustafa; van Oudheusden, Bas; Remes, Bart

DOI
10.2514/1.J055146

Publication date
2017

Document Version
Accepted author manuscript

Published in
AIAA Journal: devoted to aerospace research and development

Citation (APA)
Perçin, M., van Oudheusden, B., & Remes, B. (2017). Flow Structures Around a Flapping-Wing Micro Air Vehicle Performing a Clap-and-Peel Motion. *AIAA Journal: devoted to aerospace research and development*, *55*(4), 1251-1264. https://doi.org/10.2514/1.J055146

Post print in: AIAA Journal, Vol. 55, No. 4 (2017), pp. 1251-1264
https://doi.org/10.2514/1.J055146

Flow structures around a flapping-wing micro air vehicle performing a clap-and-peel motion

Mustafa Percin[a], Bas van Oudheusden[b] and Bart Remes[c]

The vortical flow structures generated by the flapping wings of the DelFly II micro air vehicle in hovering flight configuration are investigated using particle image velocimetry. Synchronous force measurements were carried out to establish the relation between the unsteady forces and force generation mechanisms, particularly the leading edge vortex (LEV) and the clap-and-peel motion. The formation of conical LEVs on both wings is revealed, which occurs rapidly at the start of the outstroke as a result of the wing-wing interaction. The LEVs of the outstroke interact with those of the instroke, which are shed and by mutual induction advect upstream as a vortex pair at the end of previous instroke. The LEV pairs induce a strong inflow into the region formed between the upper and lower wings during the peeling phase resulting in the formation of a low pressure region. This, together with the LEVs and a momentum increase formed by the clap, accounts for the generation of relatively higher forces during the outstroke. The cycle-averaged forces are estimated with reasonable accuracy by means of a momentum-based approach using wake velocity information with an average error of $15\ \%$**.**

I. Introduction

The growing need and associated research related to small-sized unmanned mobile platforms, for performing reconnaissance tasks in physically inaccessible and hazardous areas, have stimulated

---

[a] Post-doctoral researcher, Faculty of Aerospace Engineering, Aerodynamics Section, m.percin@tudelft.nl, Member AIAA.

[b] Associate professor, Faculty of Aerospace Engineering, Aerodynamics Section, b.w.vanoudheusden@tudelft.nl, Member AIAA.

[c] Researcher, Faculty of Aerospace Engineering, Control and Simulation Section, b.d.w.remes@tudelft.nl

bio-inspired designs, particularly in the field of micro air vehicles (MAVs). This is mainly due to the reduced performance of conventional modes of flight (fixed-wing and rotary-wing) in terms of aerodynamic efficiency and maneuverability at the intended flight regimes [1–6], which are characterized by low Reynolds numbers (Re) at the order of 10^4-10^5 [7]. On the other hand, biological flyers, such as small birds and insects, show exceptional performance in the low Re flight regimes by flapping their wings. The superior performance arises from a combination of several unconventional and complex unsteady aerodynamic mechanisms, most prominent of which are the formation of a leading edge vortex (LEV), rotational forces, clap-and-fling motion, wake capture [8–10]. Among these, the LEV has received considerable attention and it has been subject of many investigations, using either robotic flapping mechanisms [11–17] or through experimentation on flapping-wing animals [18–22]. Another important mechanism is the clap-and-fling motion, which is the wing-wing interaction that can occur during the stroke reversal in the case of large stroke amplitude or in the case of bi-plane flapping wing configuration. The underlying force enhancement mechanisms have been proposed as: 1) attenuation of the starting vortex formation at the start of the fling [9]; 2) downward momentum jet at the end of the clap; 3) generation of a massive LEV [23]. It was further shown that wing flexibility plays an important role in enhancing the aerodynamic efficiency of the clap-and-fling motion [24]. This can be attributed to different morphology of the flexible wings during the flapping motion such that the fling occurs more like a peel and the clap more like a reverse peel [25]. For this reason, it is referred to as clap-and-peel motion for the case of flexible wings.

The aforementioned mechanisms have also been exploited in several bio-inspired flapping-wing MAVs [3, 26], one of which is the DelFly [27, 28]. The different design variants all have a bi-plane wing configuration in common, that exhibit a clap-and-fling type flapping motion (Fig. 1). The significance of the unsteady aerodynamic mechanisms in the DelFly operation has been investigated in a number of experimental studies by means of quantitative flow visualization using particle image velocimetry (PIV). The measurements were performed with the DelFly II (with a wing-span of 28 cm and a nominal mass of 17 g, henceforth referred to as the DelFly) and the DelFly Micro (with a wing-span of 10 cm and a nominal mass of 3 g) configurations of the DelFly flapping-wing MAV

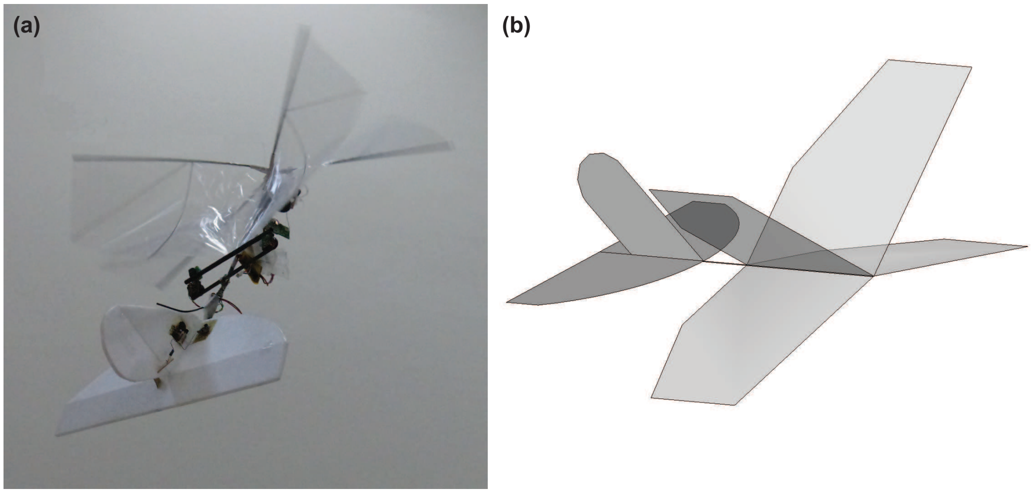

Fig. 1 a) DelFly II in flight, b) sketch of the DelFly II

family. Although the unsteady wake flow structures particularly in the forward flight configuration were captured with relative ease [29, 30], it proved to be challenging to perform accurate flow measurements in the direct vicinity of the flapping wings due to a number of complicating factors: (1) the shiny wing surface which is built from Mylar foil and causes significant reflections and glare once the vicinity of the wing is illuminated to perform PIV measurements; (2) the considerable amount of unsteady wing deformation that results in the time-variation of light blockage and reflection in the flow field; (3) the presence of two wings on each side of the fuselage that also interact with each other. All these factors can result in optical obstructions and saturation of the images in the vicinity of the wing due to glare and reflections, that may hinder the visualization of the LEV, as reported by de Clercq [31]. She performed time-resolved stereoscopic PIV (stereo-PIV) measurements around the wings of a DelFly model flapping at 13 Hz in hover configuration and showed that there is a strong influx into the gap between the wings during the peel phase, whereas there is no downward expelling jet during the clap. Although she was not able to provide a clear picture of the LEV during most part of the flapping motion due to optical obstruction, its occurrence was suggested by the significant augmentation in lift generation. Later, Groen [32] performed phase-locked stereo-PIV measurements to capture the flow fields in the vicinity of the flapping wings. In order to reduce the effects of the optical obscurities and laser-induced reflections, the illumination plane was aligned normal to the upper wing surface for a given phase of the flapping motion. By this approach, the existence of an LEV during the flapping motion of the DelFly was revealed explicitly for the first time. The measurements were done also at different spanwise positions and it was shown that the LEV has a conical shape increasing in size from root to tip, up to approximately 86 % of the wing span. It was speculated that at this location, the LEV tube connects to the tip vortex and is bent toward the trailing edge.

In addition to aforementioned experimental researches performed on the DelFly flapping-wing MAV, there are also other studies in the literature that have aimed to explore the flow structures and force generation of flapping wings. Generally, the flapping motion is achieved by use of a robotic model with MAV-scaled wings, which cannot fly by itself but can mimic complex insect-based wing kinematics and operate at similar Reynolds numbers with the MAVs or some simplified theoretical aerodynamic models are utilized in order to assess the aerodynamic performance. Tarascio et al. [33] performed a flow-visualization study on a flapping rigid rectangular wing driven by such a mechanism. They covered the wings and driving mechanism with a thin black coating (~ 0.02 mm) to reduce laser-induced reflections and glare. Consequently, they reported the presence of multiple vortices on the top surface of the wing during the translation phase of the motion. They showed that the LEV grows in the spanwise direction and that the flow is rather separated at the outboard sections of the wing. Seshadri et al. [34] conducted an experimental study employing a rigid rectangular wing driven by a mechanism that is capable of emulating complex insect wing flapping kinematics. As a result of PIV and force measurements, they identified a strong LEV responsible for the significant increase in forces. They also pointed out that the strength of the LEV varies during the flapping cycle. Ansari et al. [35] used a non-linear unsteady aerodynamic model [36, 37] with motion kinematics inspired from two-winged flies (*Diptera*) in order to investigate the effect of wing geometry on the aerodynamic performance of hovering insect-like flapping wings. They reported that the best performance occurs with the wings that have straight leading edges and a high aspect ratio with a significant wing area at the outboard locations where flow velocities are higher. Ramananaviro et al. [38] used a self-propelled flapping flyer model with wings of varying chordwise flexibilities in order to study the influence of wing deformation on the aerodynamic performance. They incorporated a simplified forced oscillator model in order to obtain the dynamics of the wing structure and revealed that the optimum aerodynamic performance is more likely to be achieved by adjusting the wing shape during the flapping cycle rather than occurrence of structural resonance which has been suggested to amplify the flapping amplitudes with less effort. The clap-and-peel mechanism and the associated wing-wing interaction have also been subject to research in a number of experimental and numerical studies. Lehmann et al. [23] performed instantaneous PIV and force measurements on dynamically scaled rigid fruit fly wings to explore the effects of the clap-and-fling motion on the force production. They pointed out that clap-and-fling motion, depending on the stroke kinematics, may enhance the force production up to 17 %. As to the responsible mechanism, detailed flow field analysis revealed that the presence of the bilateral image wing elevates the circulation induced by the leading edge vortex at the onset of the fling phase, obviously correlated with a prominent peak in both lift and drag. Moreover, it was shown that trailing edge vorticity shed during the clap phase is significantly reduced with respect to the single flapping wing case.

Evidently, flow field measurements around flapping wings of a more realistic MAV configuration, such as the DelFly is not as straightforward as for these more generic setups due to the aforementioned reasons, however, obtaining information about the formation and behaviour of the LEV is of great importance for understanding the role of these force generation mechanisms for the MAV under study. In the case of the DelFly, the presence of the mirror wing and the wing-wing interaction occurring during the stroke reversal from instroke to outstroke (clap-and-fling motion) influences the formation of the LEV as well as possibly generating a jet-flow as a result of the clapping motion. In this respect, it is aimed to explore the evolution of unsteady flow structures in the vicinity and wake of the DelFly II flapping wings in hover configuration via PIV measurements, which has improved our ability to analyze flapping-wing aerodynamics by allowing to obtain flow fields resolved in time and space [39]. Different from previous investigations on the DelFly, the wings were sprayed with a mat black paint to avoid excessive reflection caused by the Mylar foils. The PIV measurements were performed in two different configurations to capture the flow fields both around and in the wake of three flapping-wing configurations with different aspect ratios (AR). The flow field measurements were complemented with simultaneous force measurements in order to establish the relation between the evolution of forces and the flow structures.

II. Experimental setup and data processing

A. Experimental setup

The experiments were performed in a quiescent environment (simulating the hovering flight configuration) with a full-scale DelFly II model without a tail, which was mounted on a balance system that also consists of an ATI Nano-17 Titanium force sensor and variable pitch and yaw mechanisms. For the hovering flight configuration, the force in the x_b direction of the body coordinate system (see Fig. 2a) is the focus of interest because it is the force component (which will be referred to as the X-force) that balances the weight of the DelFly (viz. the lift for hovering configuration). The force sensor is calibrated to have a maximum sensing value of 32 N in x_b, y_b and 56.4 N in z_b direction with a measurement uncertainty of 1% of the full-scale load with 95% confidence level. The data acquisition and synchronization system consists of two main subsystems: (1) an in-house developed microcontroller system for the regulation of the flapping frequency and the synchronization of the force measurements and the image acquisition for the PIV measurements; (2) an in-house programmed Field-Programmable Gate Array (FPGA) system of National Instruments (NI) for the data acquisition. The microcontroller system counts the electrical commutations of the brushless DelFly motor for high-resolution rotational information and reads a Hall sensor with its magnet placed on the wing driving gear of the model for zero-referencing. Based on this information, the system then regulates the power supplied to the DelFly motor with a very slow integrator-only controller to keep the average flapping frequency constant on the long run. The FPGA system features analog input modules (NI 9239) to acquire the motor commutation information, the Hall sensor signal, voltage and current fed to the brushless motor as measured in the microcontroller system in addition to two bridge analog input modules (NI 9237) to acquire the six components of forces and moments at a given data acquisition frequency. The power consumption of the DelFly is calculated by multiplying the time-resolved measured values of voltage and current supplied to the wing-driving system. In the present experiments, the data were captured at a recording rate of 10 kHz. The test were performed for flapping frequencies (f) in the range of 9-12 Hz.

A Chebyshev II low-pass filter with -80 dB attenuation of the stop-band was used to filter the

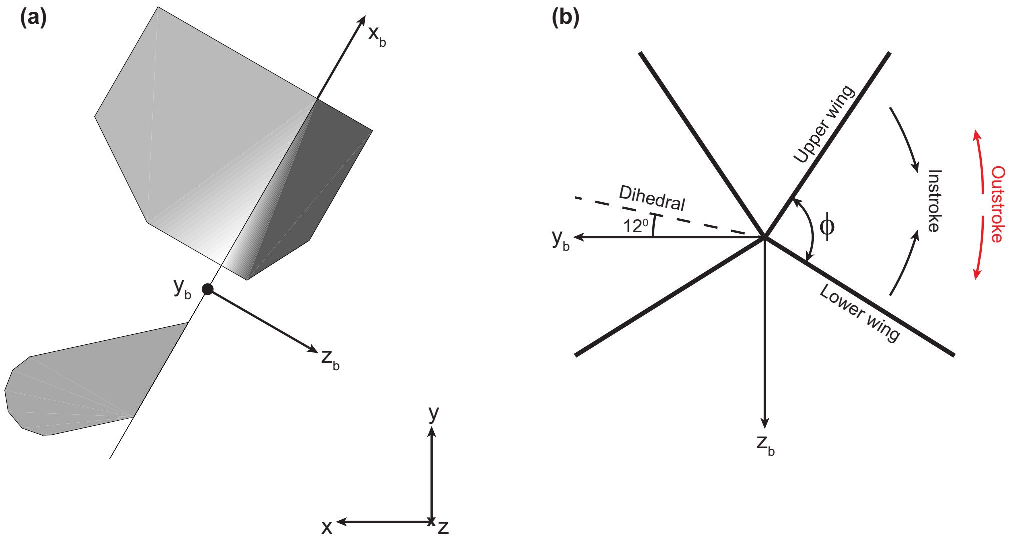

Fig. 2 a) Inertial (x, y, z) and body (x_b, y_b, z_b) coordinate systems, b) front view of the wing leading edges

Table 1 Properties of the tested wing configurations

Name	Membrane thickness (μm)	b (mm)	$\overline{c}$ (mm)	S (mm^2)	AR
Ref	10	280	80	22390	3.5
HAR	10	320	80	25589	4
LAR	10	240	80	19191	3

raw force data in MATLAB (with a forward-backward filtering technique to prevent time shift of data). The cut-off frequency was selected based on the flapping frequency to preserve only the first two harmonics of the X-force as these were found to be related to aerodynamic forces [40].

Three wings were tested in the experimental campaign. The wings are built from Mylar foil with a thickness of 10 μm, a D-shaped carbon rod (1.4 mm × 0.7 mm) and carbon rods of 0.28 mm diameter to form the leading edge and stiffeners, respectively (the reader is referred to [27, 28] for detailed information). The standard wing layout is used as the reference wing layout (referred to as Ref, see Fig. 3a). Then the reference wing was scaled up and down in the spanwise direction to produce the high aspect ratio (referred to as HAR, Fig. 3b) and the low aspect ratio (referred to as LAR, Fig. 3c). The properties of these wing configurations (b being the span length, $\overline{c}$ the mean chord length and S the total wing area) are given in Table 1.

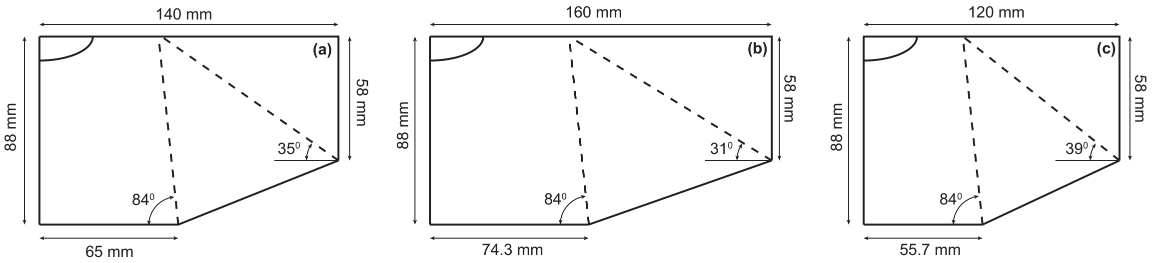

Fig. 3 Wing layout with stiffener orientation and location of a) the standard (Ref), b) the high aspect ratio (HAR) and c) low aspect ratio (LAR) wings

B. Time-resolved particle image velocimetry

Two different PIV measurement arrangements were used in order to obtain the evolution of flow structures around and in the wake of the flapping wings. Three high-speed cameras (Photron FASTCAM, SA 1.1) were employed equipped with 60 mm Nikon lenses mounted on Scheimpflug adapters where required. The flow region under investigation was illuminated by a double- pulsed Nd:YFL laser (Quantronix Darwin Duo, wavelength, 527 nm). The laser sheet thickness was around 2 mm. A SAFEX fog generator (DANTEC DYNAMICS Inc.) was used to generate a water-glycol based fog of droplets with a mean diameter of 1 μm. Double-frame images of tracer particles were captured at a recording rate of 200 Hz. A total of 200 to 600 images were taken for each measurement condition, such that in each case at least 10 flapping cycles are captured. By doing so, images from different flapping cycles with the same wing-beat frequency can be used to resolve one period with more non-dimensional time instants.

The first setup was configured to acquire time-resolved flow fields around the wings on one side of the DelFly. In this configuration, the measurement plane (laser plane) was oriented in the chordwise direction and illuminated from the front as illustrated in Fig. 4a. The cameras were arranged in the same horizontal plane as the experimental model at an angle of 40° with respect to each other. The three-camera setup was configured primarily for the stereo-PIV measurements. However, excessive reflections from the wing surface (particularly for the second camera as it was in the forward scattering mode) and optical obstruction (particularly for the third camera, vision of which was blocked by the wings) made it difficult to perform accurate stereoscopic calculations out of the three camera images for most phases of the flapping motion. Therefore, a planar-PIV

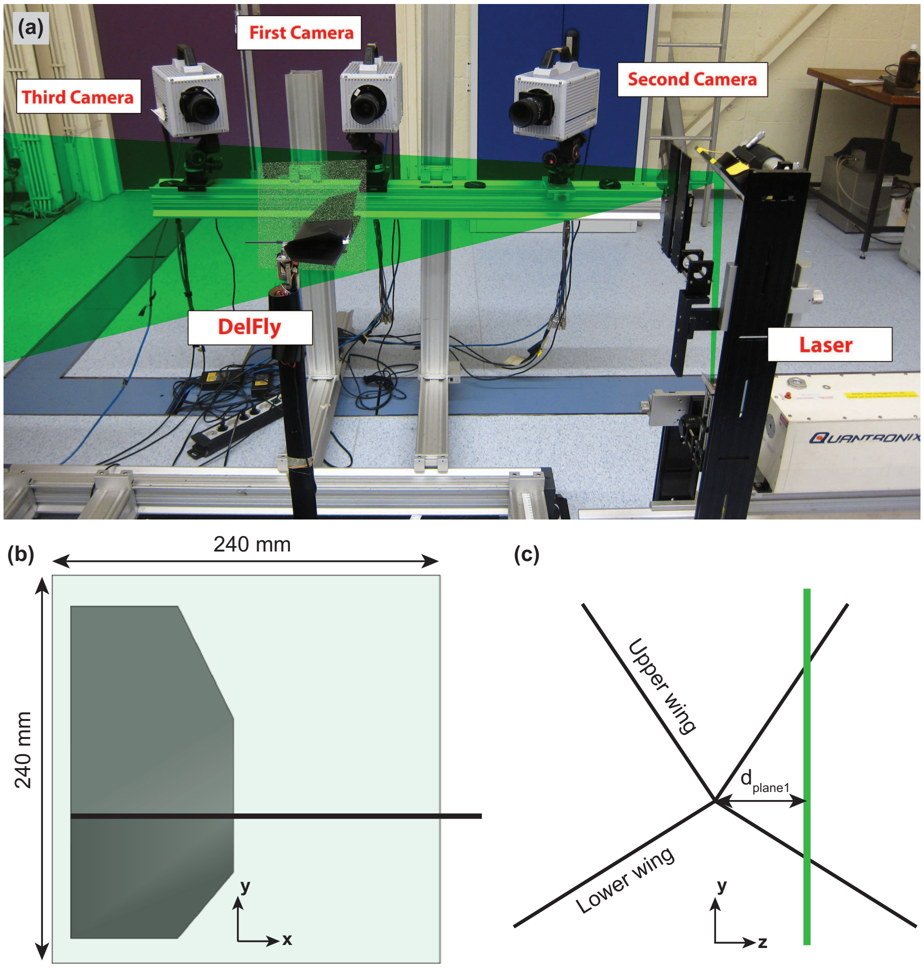

Fig. 4 a) First experimental setup to acquire time-resolved velocity fields in the vicinity of the flapping wings, b) sketch of the side view of the DelFly model with the measurement plane for the planar-PIV measurements, c) sketch of the front view of the DelFly model with the orientation of the measurement plane

approach was then followed using the images from the first camera, which was aligned normal to the laser plane. In this case, the field of view is 240×240 mm^2 (Fig. 4b) that was captured with a magnification factor of 0.85 at a digital resolution of 4.2 pixels/mm. The measurements were performed at 8 spanwise positions in a range from 40 to 180 mm distance from the wing root (d_{plane1}, see Fig. 4c). The laser plane was kept fixed and the complete balance mechanism was shifted with increments of 20 mm to perform the measurements at different spanwise locations.

In the second arrangement, the laser plane was again aligned in the chordwise direction to capture the evolution of the spanwise oriented vortical structures, i.e., LEVs and trailing edge

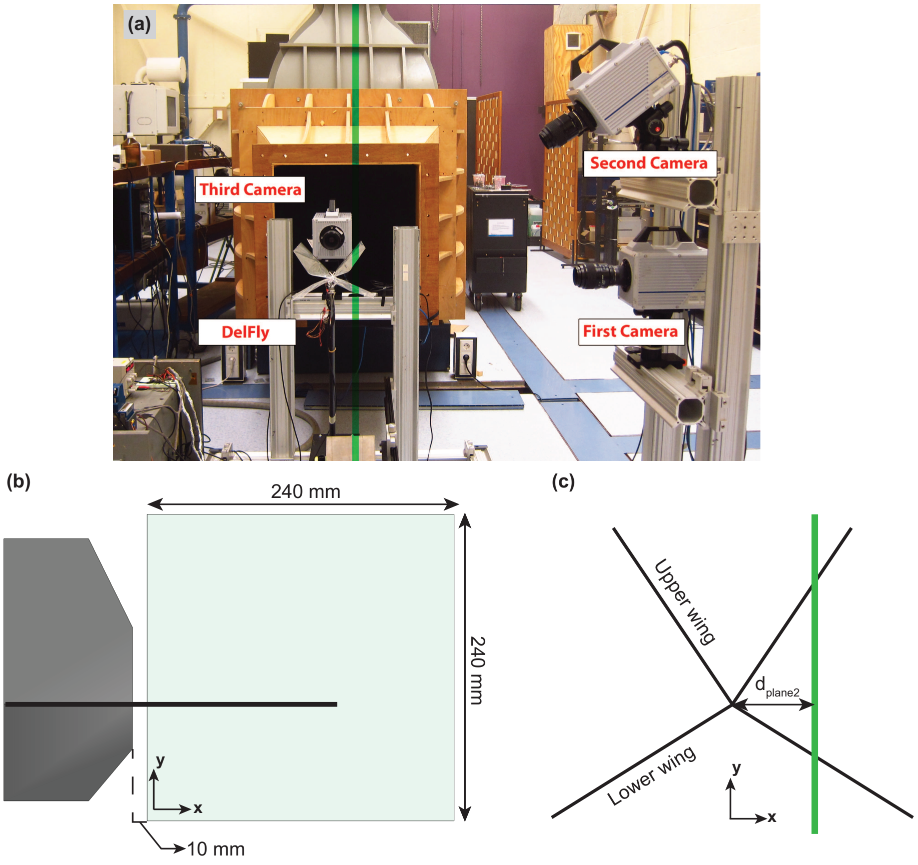

Fig. 5 a) Second experimental setup to acquire time-resolved velocity fields in the wake of the flapping wings in the chordwise oriented measurement planes, b) sketch of the side view of the DelFly model with the measurement plane for the stereo-PIV measurements, c) sketch of the front view of the DelFly model with the orientation of the measurement plane

vortices (TEVs), in the wake of the flapping wings (Fig. 5a). The measurement region was a square plane with the dimensions of 240×240 mm^2 (Fig. 5b) that was captured at a magnification factor of approximately 0.85. The measurement region was centered about an axis slightly above the fuselage of the DelFly model to cover the complete stroke amplitude of the wings and located at 10 mm downstream position from the trailing edge of the wings. The stereo-PIV measurements were performed at 10 spanwise positions by use of 2 high-speed cameras. The first measurement plane was aligned at 20 mm distance from the wing root (d_{plane2}, see Fig. 5c) on the right hand side of the model and the complete setup was shifted with an increments of 20 mm up to 200 mm from the wing root while keeping the laser plane fixed fo perform the measurements at different spanwise positions. The first camera was positioned at the same horizontal plane with the DelFly model, whereas the second camera was located above the model at 40° angle with respect to the first camera. The third camera was aligned at a normal view to the flapping wings in order to acquire the phase angle of the wings at the PIV image acquisition instants.

The commercial software Davis 8.1.6 (LaVision) was used for the PIV data acquisition, image pre-processing, stereoscopic and planar correlation of the images, and further vector post-processing. For both around-wing and in-wake measurements, the pre-processed double frame images were interrogated using windows of final size of 64×64 pixels with two refinement step and an overlap factor of 75 % resulting in approximately 4096 vectors with a spacing of 3.8 mm in each direction.

III. Results and Discussion

A. Flow structures around the flapping wings

The aim of the around-wing measurements is mainly twofold: (1) to reveal the formation and subsequent behaviour of the spanwise oriented vortical structures (i.e., LEVs and TEVs); (2) to relate the vortex dynamics to the X-force generation.

The resultant vector fields were overlapped with the corresponding image recordings of the camera to provide a combined view of the vortical structures with the position and the shape of the wings at the same time. In these images, black bands are used to mask the regions, which suffer from lack of illumination due to blockage of the wings or excessive reflection of the laser light. The vortices are labeled in order to better follow their behaviour throughout the images: each label reports the typology (LEV or TEV), the stroke phase (in and out for instroke and outstroke, respectively) and the wing to which they belong to (u and l for upper and lower, respectively). The stroke angle (Φ, see Fig. 2b) and the non-dimensional time ($t^* = t \times f$, where t is the time in seconds) are used to define the phase of the presented flow fields. The start of the instroke ($\Phi = 87^\circ$) is defined as the beginning of the flapping period ($t^* = 0$).

Before proceeding to further discussion, there are some points that should be mentioned to facilitate interpretation of the results. The planar-PIV measurements in this case are used to visualize the vortical structures rather than providing a quantitative information due to two reasons: (1) the fixed vertical measurement plane does not intersect the wings at the same nominal spanwise position and at a right angle during the wing-beat cycle due to the curvilinear nature of the flapping motion; (2) the reflection of the laser light prevents proper measurements close to the wing surface. Due to the former, the angle between the transverse vortical structures and the measurement plane varies in time which results in the sampling of a vortex in sectional planes that are not perpendicular to the main axis of the vortex at a given spanwise location. Furthermore, due to dihedral angle of the wings, the relative orientation of the upper and lower wings with respect to the measurement plane is different at a given phase of the flapping motion. This hinders the comparison of vortical structures of the two wings in terms of their strength at a particular measurement instant.

Contours of non-dimensional out-of-plane vorticity (ω_z/f) are plotted in a plane that is located at 100 mm from the fuselage of the DelFly (d_{plane1} = 100 mm) for six instants during the flapping cycle, for a flapping frequency of 11.2 Hz (Fig. 6). For this particular case, the flap-averaged X-force is approximately 0.17 N, which is sufficient to support the weight of the DelFly in hovering configuration. The measurement plane position corresponds to approximately $0.73R$ when the stroke angle is zero (i.e., when the wings are fully closed at the end of instroke). At the flapping instant A (t^* = 0.13 and Φ = 53.8°), the wings are moving in the instroke direction with the leading edge vortices ($\mathrm{LEV}_{\text{in-u}}$ and $\mathrm{LEV}_{\text{in-l}}$) visible in the vicinity of the wing leading edges. The trailing edge vortices of the previous instroke ($\mathrm{TEV}_{\text{in-u}}$ and $\mathrm{TEV}_{\text{in-l}}$) are still present in the far wake. There are also relatively small-scale vorticity contours in the near wake, which are probably the LEVs and TEVs of the outstroke phase. The time stage B (t^* = 0.28 and Φ = 28.9°) corresponds to the maximum X-force generation instant during the instroke phase. The LEVs are now more elongated along the surface of the wings. A close inspection on the lower wing, which is oriented almost perpendicular to the measurement plane at this time instant, reveals that the positive vorticity contours cover the complete wing surface. At the start of the outstroke (C, t^* = 0.49 and Φ = 1.0°), the wings are nearly in their non-deformed state and parallel to each other. At this stage of the motion, the X-force generation is at the local minimum level between the force peaks of the instroke and the outstroke. This can be attributed to the wings being relatively stationary and their small surface area oriented in the streamwise direction, which also results in better illumination conditions in the wake and provides a clear picture of the wake structures. The LEVs generated during the instroke ($\mathrm{LEV}_{\text{in-u}}$ and $\mathrm{LEV}_{\text{in-l}}$) are shed and moved upstream with their induced velocities in the

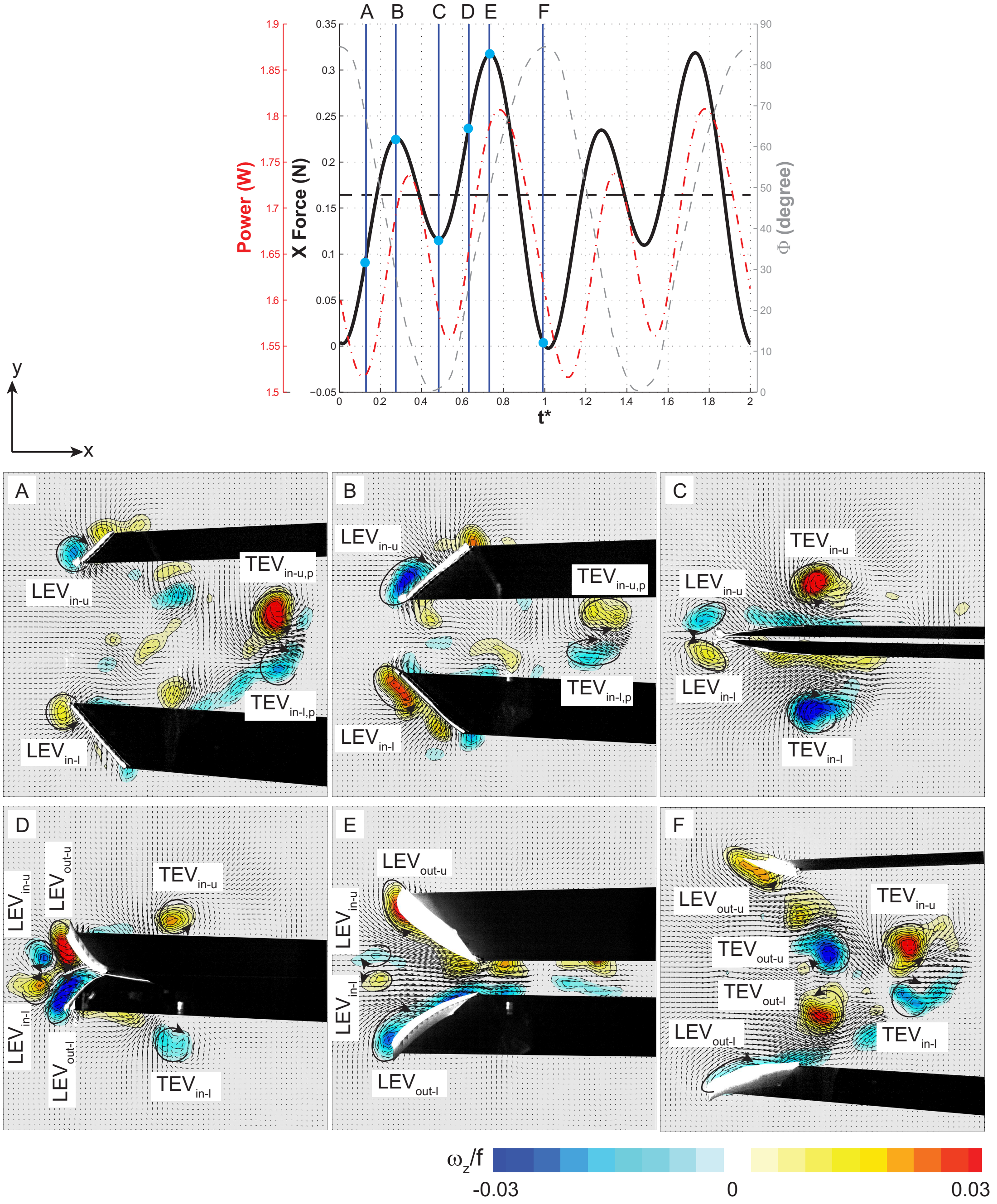

Fig. 6 Temporal variations of the X-force (*black line*) and power consumption (*dash-dot red*) plotted for two periods of the flapping motion for the flapping frequency of 11.2 Hz in hover configuration of the DelFly with Ref wings complemented with the variation of the stroke angle (Φ, *dashed gray*) and the flap-averaged X-force value (*dashed black*)(*top*); contour plots of the non-dimensional out-of-plane vorticity (ω_z/f) in a chordwise oriented plane at 100 mm distance from the fuselage ($d_{\mathbf{plane1}}$ = 100 mm, see Fig.4c) at six instants of the flapping cycle (A at t^* = 0.13 and Φ = 53.8°, B at t^* = 0.28 and Φ = 28.9°, C at t^* = 0.49 and Φ = 1.0°, D at t^* = 0.63 and Φ = 27°, E at t^* = 0.73 and Φ = 51°, F at t^* = 0.98 and Φ = 85°)

form of a vortex pair. The trailing edge vortices generated during the instroke phase ($\mathrm{TEV}_{\text{in-u}}$ and $\mathrm{TEV}_{\text{in-l}}$) are present in the wake forming a horizontally-oriented mushroom-type vortical structure. This vortical formation in combination with the clapping motion of the wings induces a positive streamwise velocity and generates a momentum-surplus wake velocity profile, which is evident from the contours of positive non-dimensional streamwise velocity ($V_x/V_{m,tip}$) in the near wake of the wings as shown in Fig. 7. On the other hand, the LEV pair induces a negative streamwise velocity which results in a slight momentum-deficit at the upstream conditions. This net momentum increase is indicative of force generation in the negative x direction (i.e., positive X-force in the DelFly body coordinate system). Indeed, the comparison of the force generation levels of the flapping motion at the two stroke reversals shows that the X-force is significantly higher while turning from instroke to outstroke. This can be explained by the formation of a streamwise momentum jet (i.e., downward momentum jet in the case of actual hovering orientation) by the wing-wing interaction (clapping motion) and the interaction between the flow structures of the upper and lower wings. As the motion progresses in the peeling phase (D, $t^* = 0.63$ and $\Phi = 27^\circ$), two massive LEVs ($\mathrm{LEV}_{\text{out-u}}$ and $\mathrm{LEV}_{\text{out-l}}$) appear in the gap between the two wings, which occupy the peeled wing surface regions of both wings completely (note that the lower wing intersects the measurement plane at nearly a right angle also at this phase of the flapping motion so that presumably the $\mathrm{LEV}_{\text{out-l}}$ is also cut nearly at a right angle). The rapid build-up of circulation for the LEVs can be attributed to the inrush of the surrounding fluid into the low-pressure region formed between the two wings as they peel apart (see the corresponding plot in Fig. 7). The LEVs of the instroke interact with the newly formed LEVs of the outstroke and generates a dynamic region ahead of the flapping wings. First, the LEVs of the instroke and outstroke for both wing induce a velocity component directed toward the cleft between the wings. Second, the vortex pairs of the two strokes induce velocities in the opposite direction along the mid-line of the wings: the $\mathrm{LEV}_{\text{in-u}}$ and $\mathrm{LEV}_{\text{in-l}}$ induce a negative V_x velocity in the region between them, whereas those generated at the beginning of the outstroke induce a positive V_x velocity, which results in the formation of a small region where two velocity components cancel each other out. As a result, these two effects form a tilted v-shaped streamwise velocity pattern that elongates into the gap between the wings (see Fig. 7-D).

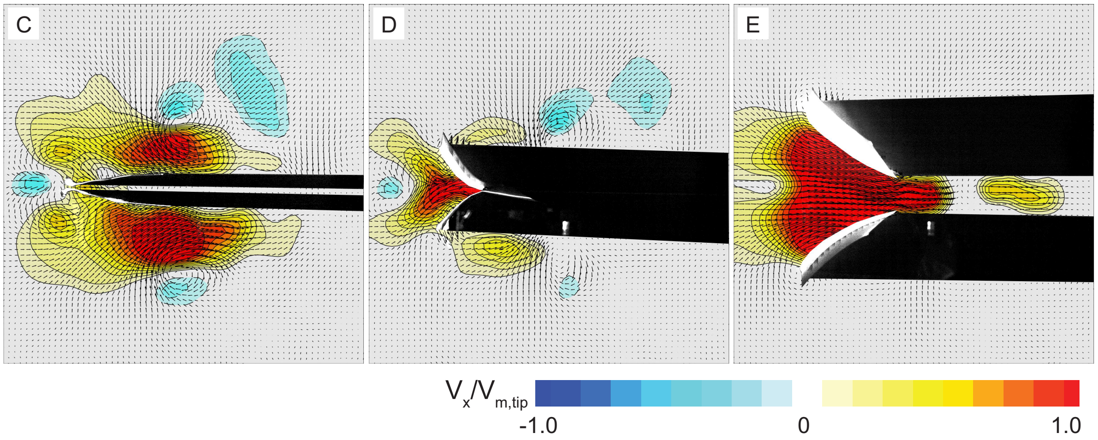

Fig. 7 Contour plots of the non-dimensional streamwise velocity ($V_x/V_{m,tip}$) in a chordwise oriented plane at 100 mm distance from the fuselage ($d_{\mathbf{plane1}}$ = 100 mm, see Fig.4c) at three instants of the clap-and-fling phase for the DelFly with Ref wings flapping at 11.2 Hz

The influence of the instroke LEVs on the force production at the beginning of the outstroke can be evaluated in different aspects. First, the presence of a counter-rotating vortex in the vicinity of the wing may inhibit the growth of the new LEV and may cause a delay in the production of forces, analogous to the Wagner effect. On the other hand, the resultant induced velocity region may also create relatively favourable conditions in terms of force generation by aligning the entrained velocity vector with the wings and preventing excessive decrease of the effective angle of attack of the wings in the stroke direction (i.e., y direction). The maximum force generation occurs at the instant E (t^* = 0.73 and Φ = 51°). The LEVs of the instroke are still situated in front of the flapping wings but their vorticity levels are clearly reduced at this stage. In relation to this, the negative velocity region induced by this vortex pair has also vanished, which is evident in Fig. 7. There is a strong inflow pattern toward the gap between the wings with magnitudes reaching the mean wing-tip velocity, which generates low pressure on the inner surface of the wings and enhancing the force production. There are two concentrated vorticity contours in the vicinity of the leading edges of the both wings representing the LEVs, but it is also evident that the associated vorticity contours elongate toward the trailing edge and even to the near wake. Probably, some amount of LEV vorticity, which is rapidly built up at the beginning of the outstroke, advects along the wing surface and sheds into the wake due to the strong flow pattern between the wings. Close to the end of the outstroke (F,

t^* = 0.98 and Φ = 85°), the X-force decreases to the minimum of the complete flapping cycle in correlation with the wings slowing down and reaching their non-deformed state. It is difficult to comment on the LEV formations at this instant due to the oblique orientation of the wings with respect to the measurement plane. However, the wake velocity field reveals that prominent TEVs form and shed during the outstroke contrary to what is hypothesized in the literature regarding the benefits of the clap-and-fling motion. It is possible that the formation of TEVs is delayed with respect to LEVs because of the fact that the trailing edges of the wings completes stroke reversal later than the leading edges as discussed in [41]. This essentially means that the lower-chord region of the wings performs a clapping motion while the leading edges move in the peeling phase.

In order to assess the spanwise variation of the flow structures, contours of non-dimensional out-of-plane vorticity are plotted in chordwise oriented planes at three different spanwise locations for t^* = 0.28 in Fig. 8. This time instant corresponds to the maximum X-force generation point of the instroke phase (B, see Fig. 6) and it is selected deliberately since the lower wing is oriented normal to the measurement plane, which will allow to assess spanwise characteristics of $\text{LEV}_{\text{in-l}}$ more accurately. It is clear that at the inner measurement plane location (d_{plane1} = 60 mm), the LEV appears rather small both in size and strength. Moreover, there is a clear evidence that the LEVs of the outstroke ($\text{LEV}_{\text{out-u}}$ and $\text{LEV}_{\text{out-l}}$) are shed and advect downstream in the region between the wings contrary to the LEVs of the instroke, which move upstream with their induced velocities at the end of the instroke. Moving toward the wing-tip, the size and circulation level of the LEV increases such that the LEV covers the complete wing surface at the outer measurement plane location, that corresponds to $0.86R$ position of the lower wing at this instant. This indicates a conical LEV structure as also reported by [42].

Comparison of the measurements at different spanwise positions at t^* = 0.63 (i.e., the other time instant when the lower wing is oriented normal to the measurement plane during the outstroke) reveals that there are prominent differences in the formation of the flow structures (Fig. 9).

First, very different TEV shedding characteristics can be observed at different measurement planes such that there are two discrete vortex structures at the innermost spanwise position (d_{plane1} = 60 mm) while no out-of-plane vorticity contours representing the TEVs at the outer spanwise position

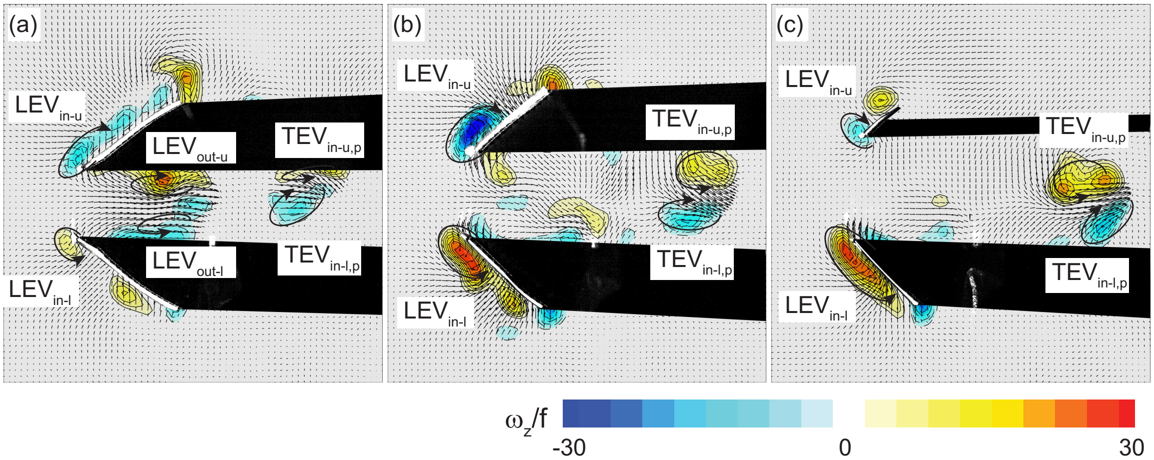

Fig. 8 Contour plots of the non-dimensional out-of-plane vorticity (ω_z/f) in chordwise oriented planes at three different spanwise positions: a) 60 mm distance from the fuselage ($d_{\mathbf{plane1}}$ = 60 mm), b) 100 mm distance from the fuselage ($d_{\mathbf{plane1}}$ = 100 mm), c) 120 mm distance from the fuselage ($d_{\mathbf{plane1}}$ = 120 mm) at $t^* = 0.28$ for the DelFly with Ref wings flapping at 11.2 Hz

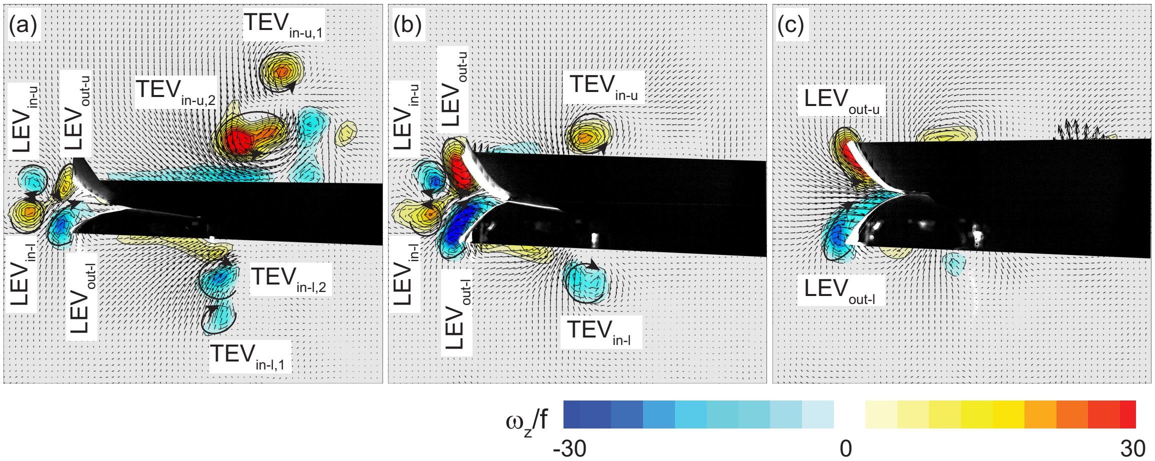

Fig. 9 Contour plots of the non-dimensional out-of-plane vorticity (ω_z/f) in chordwise oriented planes at three different spanwise positions: a) 60 mm distance from the fuselage ($d_{\mathbf{plane1}}$ = 60 mm), b) 100 mm distance from the fuselage ($d_{\mathbf{plane1}}$ = 100 mm), c) 120 mm distance from the fuselage ($d_{\mathbf{plane1}}$ = 120 mm) at $t^* = 0.63$ for the DelFly with Ref wings flapping at 11.2 Hz

(d_{plane1} = 120 mm). The large shadow region in the wake and the three-dimensional nature of the flow structures, while the measurement technique is limited to acquire velocity components in a two-dimensional plane makes it difficult to interpret this vortex shedding behaviour. Second, the LEVs of the instroke phase are found in front of the flapping wings at the first two measurements planes (viz.,

d_{plane1} = 60 mm and 100 mm) and interact with the newly formed outstroke LEVs, whereas they are not present in the outer measurement plane. Indeed, similar to the inner measurement planes, the instroke LEVs are shed and advected upstream at the previous time steps in this measurement plane, yet probably they tilt into a different direction and cannot be captured by means of ω_z visualization. The vortex tilting affects the streamwise flow pattern toward the gap between the wings as shown in Fig. 10c.

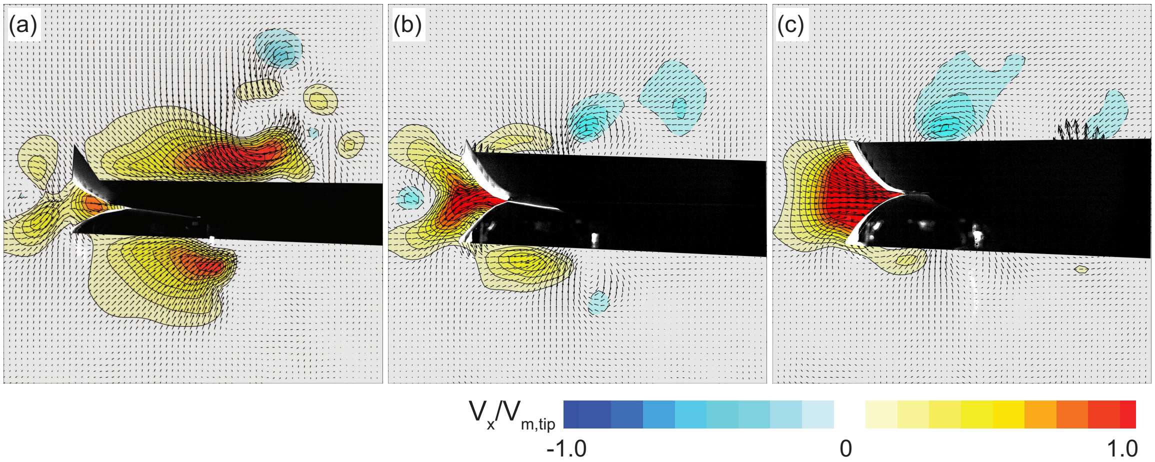

Fig. 10 Contour plots of the non-dimensional streamwise velocity ($V_x/V_{m,tip}$) in chordwise oriented planes at three different spanwise positions: a) 60 mm distance from the fuselage (d_{plane1} = 60 mm), b) 100 mm distance from the fuselage (d_{plane1} = 100 mm), c) 120 mm distance from the fuselage (d_{plane1} = 120 mm) at t^* = 0.63 for the DelFly with Ref wings flapping at 11.2 Hz

The flow pattern toward the cleft between the wing is clearly influenced by the presence and the strength of the instroke LEVs. Relatively weak instroke LEVs at the inner spanwise position cannot induce a negative velocity in the x direction. On the other hand, the absence of the counter-rotating instroke LEV pair and relatively higher wing velocity at the outer position results in a fairly uniform flow pattern upstream of the peeling wings. The increased velocity levels between the wings is basically beneficial in terms of force generation; however, this pattern probably decreases the effective angle of attack of the wings and brings about slightly decreased amount of circulation accumulated in the LEV (see $\mathrm{LEV}_{\mathrm{out\text{-}I}}$ in Fig. 9b and c).

Considering the effect of wing planform, it becomes clear from Fig. 11a that the force generation

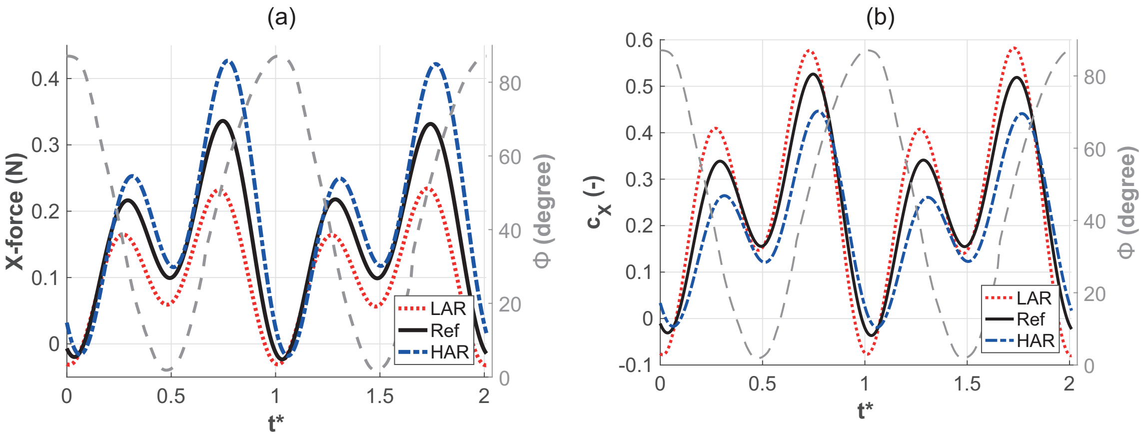

Fig. 11 Temporal evolution of the a) X-force and b) X-force coefficient (c_X) for the Ref, HAR and LAR wings at the flapping frequency of 11.2 Hz complemented with the stroke angle (ϕ) variation (*dashed gray*)

increases with the aspect ratio. This can be understood as the associated increase in wing span that increases both the wing area and the wing speed at a given flapping frequency. However, when the forces are normalized by use of the total wing area and the mean wing-tip velocity as shown in Fig. 11b, the LAR wing appears to have the highest force coefficients throughout the flapping motion. This may be attributed to different structural deformations of the wings particularly at the outboard spanwise locations. For the HAR wing, increased span length results in larger forces acting on the outboard wing area due to greater velocities, that is likely to bring about larger chordwise deformation and thus decrease of geometric angle of attack and increased wing twist, which may account for the decrease of the force coefficient. Visualization of the flow features of the HAR wings flapping at 11 Hz at a plane that is located 120 mm from the fuselage (corresponding to 0.76R position when the stroke angle is zero) at two different instants of the flapping motion (i.e., t^* = 0.28 and 0.63) reveals that qualitatively similar vortical structures are generated during the flapping motion (Fig. 12). During the instroke (Fig. 12a), prominent LEVs with comparable magnitudes to those in the Ref10 case are present near the wing surfaces. On the other hand, the instroke structures appear slightly weaker (Fig. 12b). This can be perhaps due to delayed build-up of the circulation levels, which can be inferred from the time shift in the variation of the forces. A similar time shift has been observed by Percin et al. [41] between the force evolutions of DelFly flapping wings at different frequencies such that the low flapping frequency case precedes the high frequency case. They associated this shift with the deformation characteristics of the flapping wings. Relatively higher aerodynamic forces for the high frequency case causes larger wing deformation which results in delayed stroke reversals. This accordingly brings about the delayed evolution of wing shape parameters and thus delaying the evolution of circulatory effects and forces. In this respect, the time-shift in the X-force variations for different aspect ratio wings can be attributed to different deformation characteristics of the wings such that relatively large forces acting on the outboard location of the HAR wing likely delay the evolution of wing shape, circulatory effects and forces.

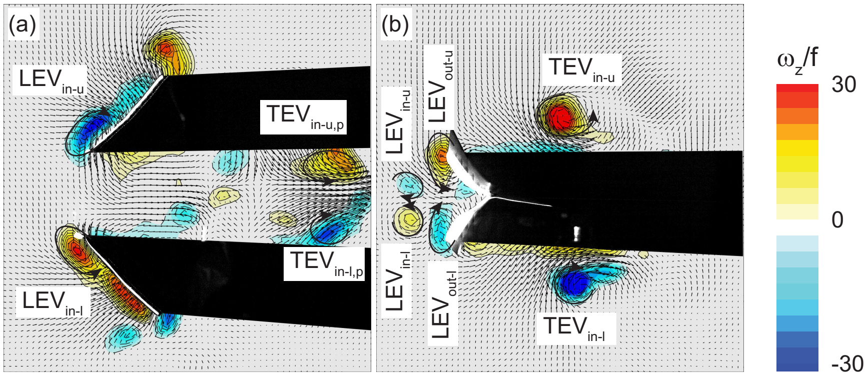

Fig. 12 Contour plots of the non-dimensional out-of-plane vorticity (ω_z/f) in a chordwise oriented plane at 120 mm distance from the fuselage ($d_{\mathbf{plane1}}$ = 120 mm) at a) t^* = 0.28 and b) t^* = 0.63 for the DelFly with HAR wings flapping at 11 Hz

B. Flow field in the wake of the flapping wings

1. *Unsteady flow structures*

Aerodynamic mechanisms in flapping-wing flight, determined by different aspects of the flapping motion such as sweeping, pitching and clap-and-peel, leave their footprints in the form of structures that are shed into the wake. In this context, the wake formations can deliver further clues about the force production characteristics of the flapping motion.

Figure 13 illustrates the evolution of wake flow structures in a chordwise oriented plane at 100 mm distance from the fuselage (d_{plane2} = 100 mm, see Fig. 5c) for the Ref wings flapping at a frequency of 11.2 Hz at four time instants in the flapping cycle (t^* = 0.28, 0.49, 0.73 and 0.98, corresponding to B, C, E and F in Fig. 6)). In order to provide a clear representation of the wake velocity profiles, velocity vectors are plotted once at every six streamwise measurement points. The region with poor imaging conditions and hence less reliable velocity vectors due to presence of the balance system is covered with a gray band in the vector fields.

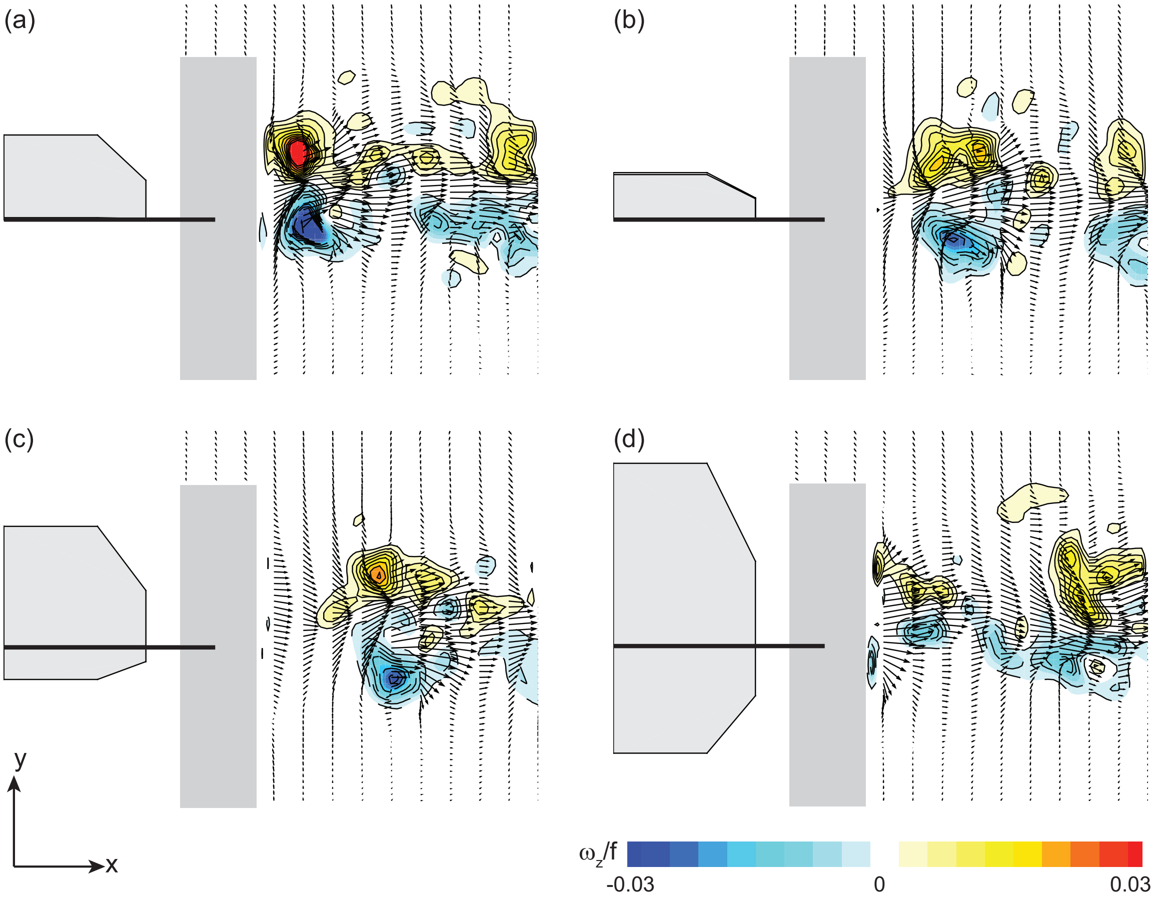

Fig. 13 Contour plots of the non-dimensional out-of-plane vorticity (ω_z/f) in a chordwise oriented plane at 100 mm distance from the fuselage ($d_{\mathbf{plane2}}$ = 100 mm) at a t^* = 0.28, b t^* = 0.49, c t^* = 0.73 and b t^* = 0.98 for the DelFly with Ref wings flapping at 11.2 Hz

In this measurement plane, there are two major flow structures present throughout the flapping motion. These are the trailing edge vortices of the upper and lower wings that are formed during the instroke and shed during the clapping phase. They convect downstream as a counter-rotating vortex pair and induce a prominent positive streamwise velocity (x-velocity) in the region between them. Their projection views on the chordwise plane grow larger and become more fragmented (compared to their coherent views at t^* = 0.28 as shown in Fig. 13a) while moving downstream and their spanwise vorticity (ω_z) levels decrease, which may be attributed to the deformation and diffusion of the wake vortices. In addition to these vortex formations, the clapping motion of the wings also induces a streamwise velocity in the form of a jet velocity profile. It is better visible at the time step of t^* = 0.98 (Fig. 13d) when the counter-rotating TEV couple is not yet in the field of view but the clap-induced jet-like velocity profile is apparent in the first vector column after the gray region. The induced streamwise velocities in this measurement plane reach approximately 1.6 times the mean wing-tip velocity during a flapping cycle in a probing point located at 1.0$\overline{c}$ distance downstream from the trailing edges of the wings (Fig. 14). The maximum velocity is achieved during the passage of the counter-rotating vortex pair so that it occurs with a phase delay at further downstream locations. In correlation with the decrease of the vorticity levels, the amplitude of the velocity oscillations also decay with downstream distance. For all three selected probe positions, the streamwise velocity shows a periodic variation indicating periodic behaviour of the wake flow structures.

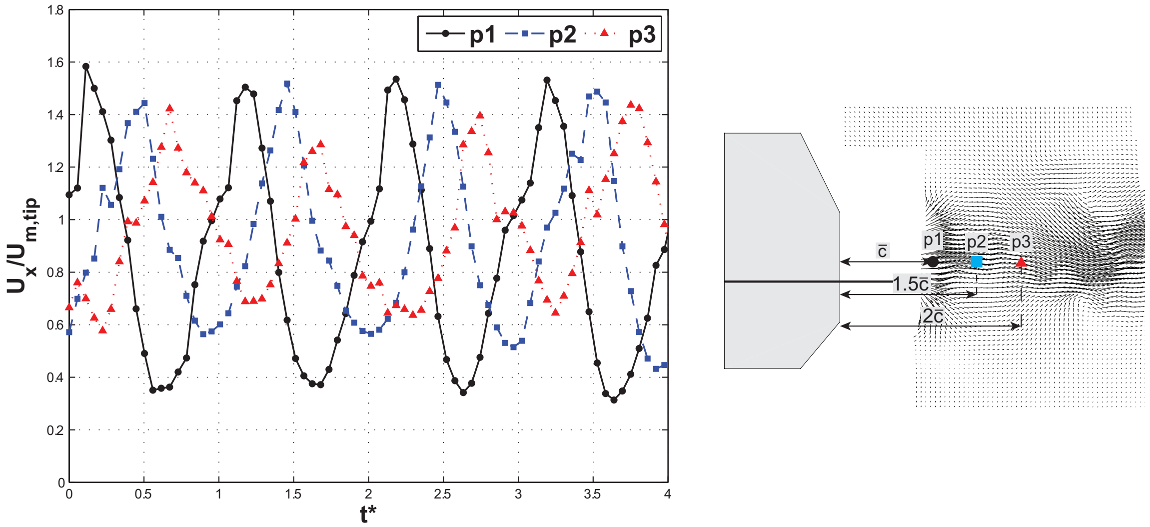

Fig. 14 Temporal variation of the nondimensional x-velocity component ($U_x/U_{m,tip}$) measured at three different streamwise positions aligned with the bisector of the wings plotted for four periods of the Ref wings flapping at 11 Hz (*left*); streamwise positions of the probe points (*right*)

In order to better visualize the wake flow structures, the three-dimensional wake structure of the flapping wings is derived from the experimental data that were captured at different spanwise locations (d_{plane2} = 20 to 200 mm). A modified Kriging regression technique [43] is utilized in order to reconstruct the three-dimensional wake with a spanwise spatial resolution that is higher than that of the PIV measurements. Wake formations for two phases of the flapping motion are shown in Fig. 15. These three-dimensional wake reconstruction results confirm the presence of a counter-rotating vortex pair (VS1) that is shed at the end of the instroke. This vortical formation is slightly tilted with respect to the z axis and aligned with the dihedral of the wings. In addition to these vortices, there is another vortical structure that is aligned rather vertically (VS2) and shed at the end of the outstroke. This arrow-shaped structure is comprised of mainly y-vorticity, thus it does not emerge in the chordwise oriented measurement planes.

2. Estimation of forces

The wake velocity information is also utilized in an attempt to estimate the aerodynamic X-force by means of a momentum-based approach. In this process, a control volume is defined (Fig. 16a) such that the upstream and downstream boundaries are assumed to be far enough to have the static pressure equal to ambient pressure. The upstream boundary is positioned at an arbitrary location with a zero-inflow assumption in view of the hovering flight configuration that is under consideration here. The location of the downstream boundary is varied from $d = 1.0\overline{c}$ to $2.7\overline{c}$ (see Fig. 16a) in order to test the convergence of the estimated forces and validity of the static pressure assumption. The upper and lower boundaries of the control volume coincide with the boundaries of the measurement region where velocities are negligibly small. The lateral control surfaces are determined by the first and the last measurement plane in the spanwise direction (d_{plane2} = 20 and 200 or 220 mm for the close-root and outer-most measurement planes, respectively) and in these locations it is assumed that the effect of the flapping motion is significantly reduced. The interior of the control volume, on the other hand, encompasses the flapping wings. Velocity vectors at the downstream control surface are acquired from the chordwise oriented measurement planes. The

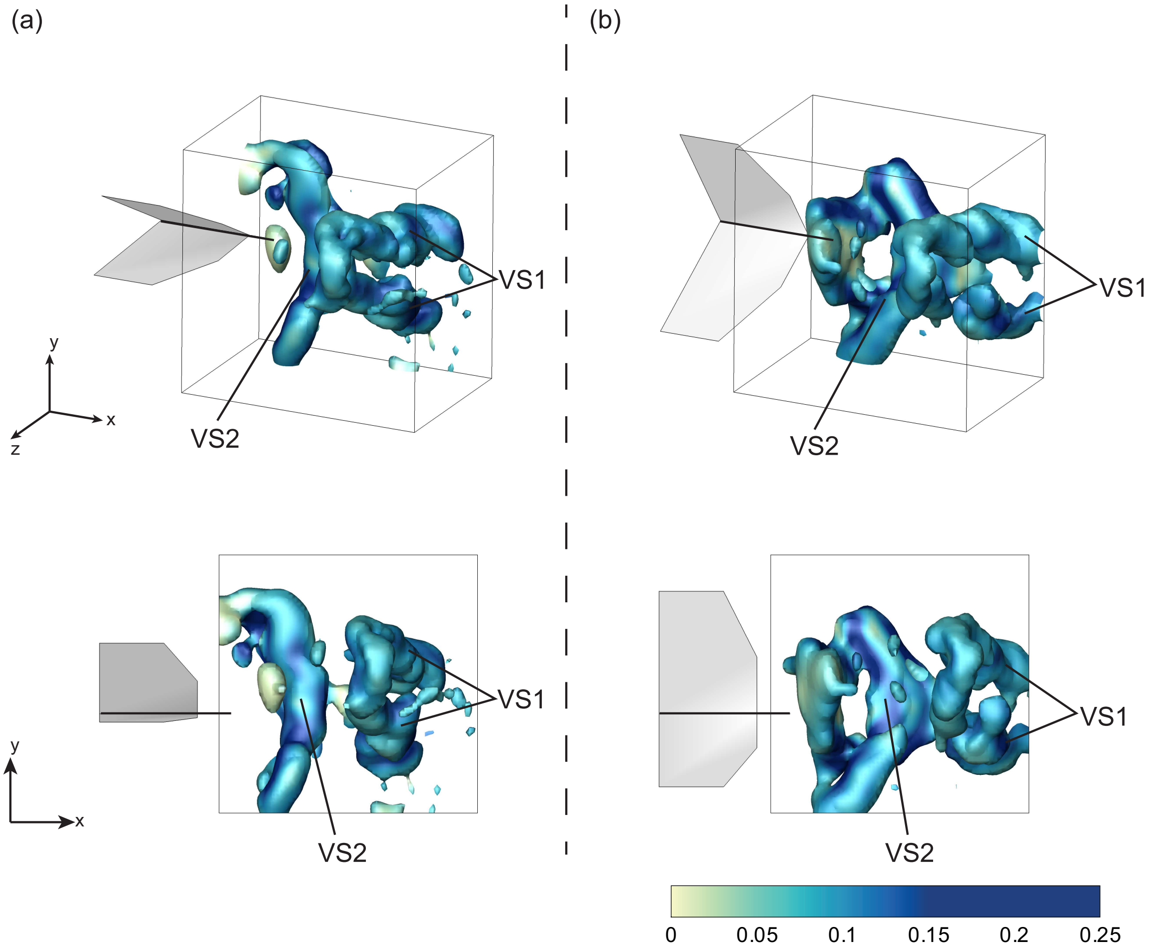

Fig. 15 Perspective (*top*) and side view (*bottom*) of the wake structures visualized by isosurfaces of $Q/f^2 = 8$ and coloured by vorticity magnitude for the DelFly with Ref wings flapping at 11.2 Hz at two instants of the flapping motion: a) $t^* = 0.6$ and b) $t^* = 0.98$

momentum equation applied to the fluid flow in the control volume reads:

$$\frac{\partial}{\partial t}\oiiint_{\mathbb{V}} \rho\vec{V}\,\mathrm{d}\mathbb{V} + \oiint_{\mathbb{S}} \rho\vec{V}\left(\vec{V}.\vec{n}\right)\mathrm{d}\mathbb{S} = -\oiint_{\mathbb{S}} p\vec{n}\,\mathrm{d}\mathbb{S} + \vec{\mathrm{F}}_{\mathrm{body}} + \vec{\mathrm{F}}_{\mathrm{viscous}} \tag{1}$$

where ρ is the fluid density, $\vec{V}$ is the velocity, $\mathbb{V}$ stands for the control volume, $\mathbb{S}$ for the control surface and $\vec{n}$ is the outward pointing normal.A number of assumptions and simplifications are made for the calculation of the X-force. Since it is assumed that pressure is equal to the ambient pressure, the first term on the right side of Eq. 1 drops out around the outer control surface. The viscous effects are also neglected for the outer boundary. Pressure and viscous forces around the inner control surface gives the total force applied to the fluid by the flapping wings. Here, the main focus of interest is the X-force component of the total force experienced by the wings, which is equal

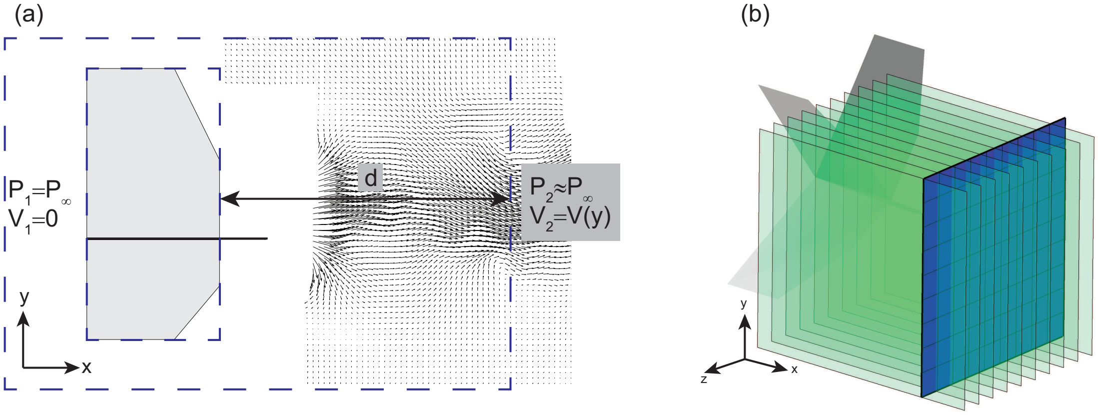

Fig. 16 a) Boundaries of the control volume (***dashed blue*** **) used for the estimation of the aerodynamic forces in a side view, b) streamwise oriented measurement planes (** ***green*** **) and downstream surface of the control volume (** ***blue*** **) formed from the velocity vectors of the measurement planes at** $2.5\bar{c}$ **streamwise distance from the trailing edge**

and opposite to that exerted on the fluid in regard to Newton's third law. It is now necessary to calculate the left hand side of the equation, where unsteady and flux terms are present, respectively. It is clear that the unsteady term requires the knowledge of the complete velocity field (particularly V_x for the calculation of the X-force) and its temporal evolution inside the control volume. As this information is not available from the present measurements, it is not possible to obtain the time-history of the forces within a flapping cycle. Instead, the flap-averaged aerodynamic X-force is determined from the averaged momentum equation, yielding:

$$\mathrm{X} = \oiint_{\mathbb{S}} \rho \left(V_{2,x}\right)^2 \mathrm{d}\mathbb{S} \tag{2}$$

where $V_{2,x}$ is velocity in the x direction measured in the downstream control surface. Note that X stands for the X-force applied on the DelFly, which is defined in the DelFly body axis (i.e., opposite to the x axis of the flow coordinate system). The X-force that is calculated by use of wake velocity profiles on one side of the DelFly is multiplied by two to account for the other half of the wake. It is noteworthy to mention that the resultant formula for the estimation of flapping-period-averaged X-force has considerable practical value since it requires velocity information only at a downstream location. However, it is still important to quantify the effects of the aforementioned assumptions. Therefore, the force estimation calculations are performed also by considering the momentum fluxes through lateral and top-bottom surfaces of the control volume.

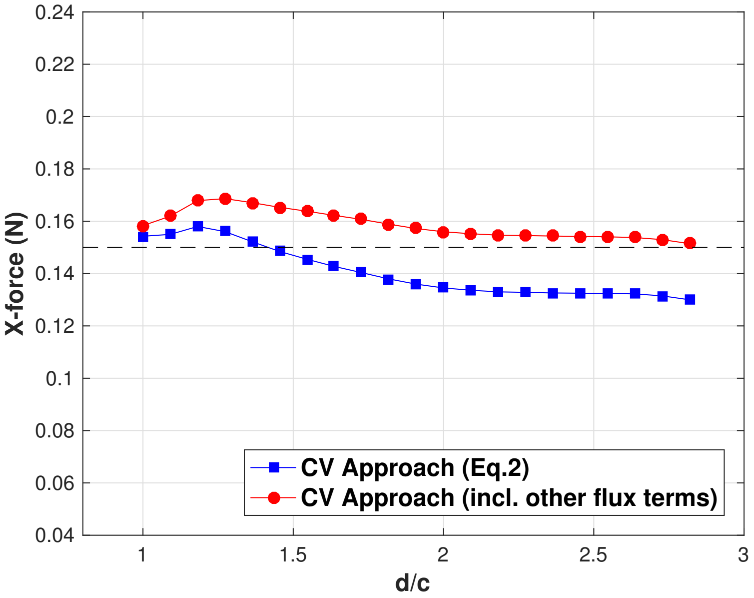

Fig. 17 Flap-averaged X-force estimated with the control volume approach by taking into account only the momentum flux through the downstream control surface (Eq. 2, *blue squares*) and considering momentum fluxes through all control surfaces (*red squares*) for the DelFly with Ref wings flapping at 11.2 Hz (black dashed-line represents the flap-averaged X-force measured with the force sensor)

Figure 17 presents the variation of the forces as a function of downstream control surface location. The estimated forces display a converging trend particularly after $d = 2\overline{c}$, while the simplified approach that considers only the momentum flux through the downstream control surface underestimates the flap-average X-force by about 12 %. On the other hand, once momentum fluxes through lateral, top and bottom surfaces are included, the prediction yields a similar force with the measured value (about 3 % higher than the measurement value). Furthermore, the comparison of the different terms reveals that the momentum flux through the downstream control surface accounts for 86 % of the total predicted force, whereas the flux through lateral surfaces contributes by 13 % for this specific case (note that the downstream boundary is placed at $d = 2.7\overline{c}$ for this analysis). Accordingly, the contribution of the top and bottom surfaces is negligible. This analysis suggests that it is required to include momentum flux through lateral surfaces for a more accurate prediction. On the other hand, it is difficult to draw strong conclusions regarding the assumption of ambient pressure at the downstream boundary since the velocity information in the lateral, top and bottom surfaces at the upstream locations from the trailing edge is not available (therefore it is assumed that there exists no net momentum flux at these locations) and the velocity data in the spanwise direction is rather coarse (with a spatial resolution of 20 mm). Nonetheless, the error levels may be considered acceptable, when the simplicity of the approach is considered. In the following parts of this section, the force predictions are performed with the downstream boundary being located at $2.7\overline{c}$ distance from the trailing edge.

The resultant flap-averaged X-force values for different wings used in the wake measurements are shown in Fig. 18. The data acquired with the force sensor is shown in black, whereas red and blue symbols represent the control volume approach calculations using only the momentum flux through the downstream control surface and all available momentum flux information (i.e., including lateral, top and bottom surfaces), respectively. In general, a good agreement in the trends is found, albeit that the simplified control volume approach results in an under-estimation of the forces. The maximum error is 18 %, which occurs for the HAR wing. The error decreases down to 14 % of the sensor-measured values for the LAR wing. When the momentum flux through the other surfaces are included in the calculations, the flap-averaged forces are estimated with a relatively higher accuracy. As mentioned earlier, this indicates that the momentum flux through lateral control surfaces should be taken into account for a more accurate calculation. In general, the momentum-based approach in a control volume for the estimation of the X-force shows a good performance, even when only the momentum flux through the downstream control surface is considered, so that it can serve as an alternative method for the determination of aerodynamic forces in flapping wing applications when direct measurements with a force sensor is not feasible (e.g., in free-flight or in cases when the sensor measurements are interfered by strong inertial components or structural vibrations).

IV. Conclusions

The temporal evolution of vortical structures around the wings and in the wake of the flapping-wing MAV DelFly has been investigated by means of two- and three-component planar PIV. Experiments were performed to acquire time-resolved flow fields around the flapping wings and in the wake, respectively. Simultaneous force measurements were conducted in order to obtain the relation

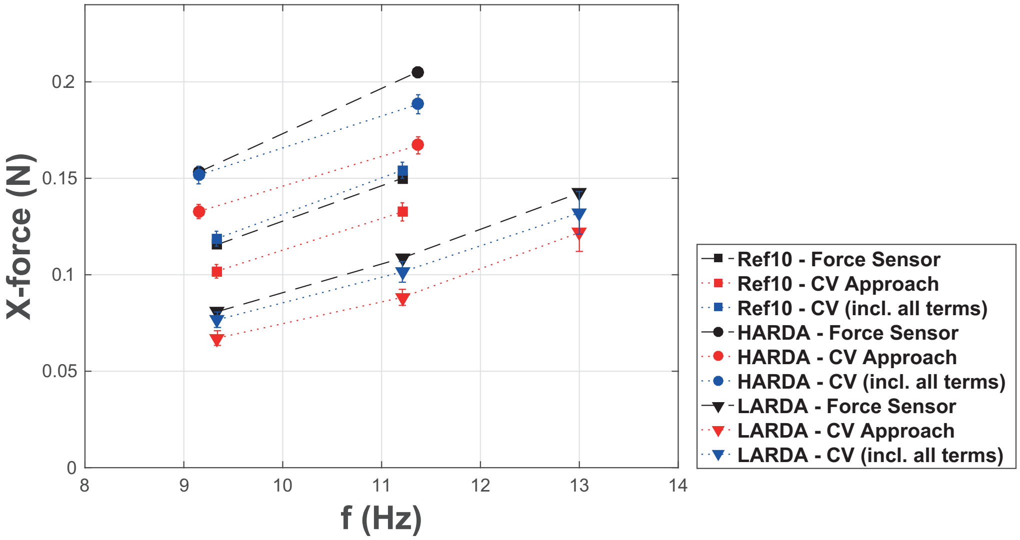

Fig. 18 Flap-averaged X-force measured with the force sensor (*black*) and estimated with the momentum-based approach in a control volume (*red*) for the Ref, HAR and LAR wings at different flapping frequencies

between the flow structures and unsteady forces. Three wing planforms of different aspect ratio were tested at various flapping frequencies.

Flow visualizations around the flapping wings reveal the presence of conical LEVs on both wings during the instroke and outstroke. The LEVs of the outstroke form and grow rapidly at the onset of this phase. They interact with the LEVs of the previous instroke that are shed and advected upstream by mutual induction. This vortex behaviour results in the modification in the streamwise velocity profile (V_x) that is generated at the beginning of the peeling phase and directed toward the cleft between the wings. This velocity component reaches a level as much as the mean wing tip velocity in the region between the wings, whereas its magnitude is significantly lowered upstream of the wings due to the induced velocities of the instroke LEVs. It is hypothesized that the particular vortex shedding behaviour and interaction between the LEVs of the instroke and outstroke prevents reduction of the effective angle of attack in the stroke direction (i.e., the sweeping motion direction). The low pressure region formed between the wings and the rapid growth of the LEVs during the peeling phase are likely reasons for the elevated forces of the outstroke. On the other hand, the formation of a momentum jet due to the clapping motion and the velocity pattern induced by the instroke TEV pair result in the generation of a momentum surplus wake, that accounts for the higher X-force generated at the end of the instroke compared to that of the outstroke.

Flow field measurements in the wake show that there are two major structures, i.e., TEVs shed from both wings during the instroke phase. They convect downstream as a counter-rotating vortex pair and induce a positive streamwise velocity in the wake. The wake velocity information has been utilized to estimate the aerodynamic X-force generated by the flapping wings with a control-volume momentum approach. The results show a reasonable agreement with the force-sensor data for all cases, even when only the momentum flux through the downstream control surface considered in the calculation (with an average error of 15 %). The average error decreases to 5 % when the momentum flux through lateral, top and bottom surfaces are also taken into account. In this respect, the momentum-based approach offers an alternative for determining the cycle-averaged force in situations when force sensor measurements are not feasible.

Acknowledgments

This work was supported by the Netherlands Technology Foundation (STW, project number 11023). The technical assistance from the MAVLab (http://mavlab.tudelft.nl/) is gratefully acknowledged.

References

[1] B. Carmichael, *Low Reynolds Number Airfoil Survey* , Technical Report NASA-CR-165803-VOL-1 (NASA, 1981).

[2] F. Bohorquez, P. Samuel, J. Sirohi, D. Pines, L. Rudd, and R. Perel, Journal of the American Helicopter Society **48**, 80 (2003).

[3] D. J. Pines and F. Bohorquez, Journal of Aircraft **43**, 290 (2006).

[4] B. R. Hein and I. Chopra, Journal of the American Helicopter Society **52**, 254 (2007).

[5] F. Bohorquez, D. Pines, and P. D. Samuel, Journal of Aircraft **47**, 268 (2010).

[6] M. Percin, *Aerodynamic Mechanisms of Flapping Flight* , Ph.D. thesis, Delft University of Technology (2015).

[7] W. Shyy, M. Berg, and D. Ljungqvist, Progress in Aerospace Sciences **35**, 455 (1999).

[8] F.-O. Lehmann, Die Naturwissenschaften **91**, 101 (2004).

[9] S. P. Sane, The Journal of Experimental Biology **206**, 4191 (2003).

[10] W. Shyy, H. Aono, S. Chimakurthi, P. Trizila, C.-K. Kang, C. Cesnik, and H. Liu, Progress in Aerospace Sciences **46**, 284 (2010).

[11] T. Maxworthy, Journal of Fluid Mechanics **93**, 47 (1979).

[12] C. P. Ellington, C. van den Berg, A. P. Willmott, and A. L. R. Thomas, Nature **384**, 626 (1996).

[13] J. M. Birch and M. H. Dickinson, Nature **412**, 729 (2001).

[14] J. M. Birch, W. B. Dickson, and M. H. Dickinson, The Journal of Experimental Biology **207**, 1063 (2004).

[15] L. Zhao, X. Deng, and S. P. Sane, Bioinspiration & Biomimetics **6**, 036007 (2011).

[16] C. W. Pitt Ford and H. Babinsky, Journal of Fluid Mechanics **720**, 280 (2013).

[17] M. Percin and B. W. van Oudheusden, Experiments in Fluids **56**, 1 (2015).

[18] R. B. Srygley and A. L. R. Thomas, Nature **420**, 660 (2002).

[19] R. J. Bomphrey, G. K. Taylor, and A. L. R. Thomas, Experiments in Fluids **46**, 811 (2009).

[20] F. T. Muijres, L. C. Johansson, R. Barfield, M. Wolf, G. R. Spedding, and A. Hedenström, Science **319**, 1250 (2008).

[21] F. T. Muijres, L. C. Johansson, M. S. Bowlin, Y. Winter, and A. Hedenström, PloS one **7** (2012), 10.1371/journal.pone.0037335.

[22] F. T. Muijres, L. C. Johansson, Y. Winter, and A. HedenstrÃűm, Bioinspiration & Biomimetics **9**, 025006 (2014).

[23] F.-O. Lehmann, S. P. Sane, and M. H. Dickinson, The Journal of Experimental Biology **208**, 3075 (2005).

[24] L. A. Miller and C. S. Peskin, The Journal of Experimental Biology **212**, 3076 (2009).

[25] C. P. Ellington, Philosophical Transactions of the Royal Society of London. Series B, Biological Sciences (1934-1990) **305**, 79 (1984).

[26] J. Sirohi, in *Engineered Biomimicry*, edited by A. Lakhtakia and R. J. Martin-Palma (Elsevier, Boston, 2013) pp. 107 – 138.

[27] G. C. H. E. de Croon, M. A. Groen, C. de Wagter, B. D. W. Remes, R. Ruijsink, and B. W. van Oudheusden, Bioinspiration and Biomimetics **7** (2012).

[28] G. de Croon, M. Perçin, B. Remes, R. Ruijsink, and C. De Wagter, *The DelFly - Design, Aerodynamics, and Artificial Intelligence of a Flapping Wing Robot* (Springer Netherlands, 2016).

[29] M. Percin, B. van Oudheusden, H. Eisma, and B. Remes, Experiments in Fluids **55** (2014).

[30] S. Deng and B. van Oudheusden, Aerospace Science and Technology **50**, 204 (2016).

[31] K. M. E. de Clercq, *Flow visualization and force measurements on a hovering flapping-wing MAV 'DelFly II'*, Master's thesis, Delft University of Technology (2009).

[32] M. Groen, *PIV and force measurements on the flapping-wing MAV DelFly II* , Master's thesis, Delft University of Technology (2010).

[33] M. J. Tarascio, M. Ramasamy, I. Chopra, and J. G. Leishman, Journal of Aircraft **42**, 385 (2005).

[34] P. Seshadri, M. Benedict, and I. Chopra, Journal of Aircraft **50**, 1070 (2013).

[35] S. A. Ansari, K. Knowles, and R. Zbikowski, Journal of Aircraft **45**, 1945 (2008).

[36] S. Ansari, R. Żbikowski, and K. Knowles, Proceedings of the Institution of Mechanical Engineers, Part G: Journal of Aerospace Engineering **220**, 61 (2006).

[37] S. Ansari, R. Żbikowski, and K. Knowles, Proceedings of the Institution of Mechanical Engineers, Part G: Journal of Aerospace Engineering **220**, 169 (2006).

[38] S. Ramananarivo, R. Godoy-Diana, and B. Thiria, Proceedings of the National Academy of Sciences **108**, 5964 (2011).

[39] R. J. Bomphrey, Evolutionary Biology **39**, 1 (2012).

[40] J. Caetano, M. Percin, B. van Oudheusden, B. Remes, C. de Wagter, G. de Croon, and C. de Visser, Bioinspiration & Biomimetics **10** (2015), 10.1088/1748-3190/10/5/056004.

[41] M. Percin, B. van Oudheusden, G. de Croon, and B. Remes, Bioinspiration & Biomimetics **11** (2016).

[42] M. Groen, B. Bruggeman, B. Remes, R. Ruijsink, B. Van Oudheusden, and H. Bijl, in *Int. Micro Air Vehicle Conf. and Competition (IMAV 2010)(Braunschweig, Germany)* (2010).

[43] J. de Baar, M. Percin, R. Dwight, B. W. Oudheusden, and H. Bijl, Experiments in Fluids **55**, 1650 (2014).